Geophysical Journal International

Geophys. J. Int. (2015) **202,** 328–346
GJI Geodynamics and tectonics

doi: 10.1093/gji/ggv139

Co-seismic vertical displacements from a single post-seismic lidar DEM: example from the 2010 El Mayor-Cucapah earthquake

Ivana Barišin,[1] Alejandro Hinojosa-Corona[2] and Barry Parsons[1]

[1]*COMET, Department of Earth Sciences, University of Oxford, Oxford, United Kingdom. E-mail: ivanab@earth.ox.ac.uk*
[2]*Department of Geology, CICESE, Ensenada, Baja California, Mexico*

Accepted 2015 March 23. Received 2015 March 8; in original form 2014 April 7

SUMMARY

A method is outlined by means of which it is possible to estimate high-resolution vertical displacements due to an earthquake even in the case where high-resolution topography is lacking before the earthquake. This result can be achieved by combining a highly accurate, post-event digital elevation model (DEM), for example lidar, with archived satellite imagery. The method is illustrated by calculating vertical displacements for the 2010 El Mayor-Cucapah earthquake. For this earthquake, there are both pre- and post-event lidar DEMs from which vertical displacements may also be estimated after correcting for the lateral advection of topography due to horizontal displacements. A comparison between the two means of deriving vertical displacements shows generally good agreement, with the displacements obtained using satellite imagery performing better in high relief areas. As a result of this property, we are able to trace the vertical offsets due to the El Mayor-Cucapah earthquake as the rupture jumped from the Pescadores fault to the Borrego fault in propagating through the high relief of the Sierra Cucapah.

Key words: Image processing; Space geodetic surveys; Continental tectonics: strike-slip and transform; North America.

1 INTRODUCTION

Measurements of surface displacements produced by earthquakes and volcanic intrusions provide invaluable information about the processes occurring at depth. Ideally, one would use a full three-dimensional displacement field to constrain earthquake mechanisms. InSAR can measure millimetric-accuracy displacements in the line of sight of the radar (e.g. Massonnet *et al.* 1993). Wright *et al.* (2004) show that a 3-D displacement field can be derived in principle by combining several InSAR data sets with different look angles. In practice, the near-polar orbits of the current SAR satellites mean that measurements are effectively only made in two distinct directions. The displacements in both horizontal dimensions may also be measured directly by image cross-correlation with sub-pixel resolution of two satellite or aerial images, one pre-event and one post-event (Leprince *et al.* 2007).

Lidar measurements of topography have recently emerged as an effective tool for studying earthquakes (e.g. Cunningham *et al.* 2006; Zielke *et al.* 2010). At present, apart from 2010 M_w 7.2 El Mayor-Cucapah earthquake, there are few other earthquakes that have lidar coverage both before and after the event (Duffy *et al.* 2013; Nissen *et al.* 2014). Nissen *et al.* (2012, 2014) obtained 3-D surface displacement fields by point-matching pre-event and post-event lidar digital elevation data on a simulated earthquake and on a real earthquake, respectively, whilst Oskin *et al.* (2012) have differenced the lidar data sets of the El Mayor-Cucapah earthquake and obtained directly the vertical displacements occurring in the earthquake. However, the study by Nissen *et al.* (2014) failed to generate a signal in the vicinity of the fault. The Oskin *et al.* (2012) study did not account for the effects on the vertical motion of the horizontal displacement produced by the earthquake, and therefore was only able to investigate displacements located on slopes of less than 3°.

In practice, because lidar measurements are costly and restricted to relatively small areas, earthquakes where there is pre-event coverage are likely to remain limited in number. However, once the earthquake has occurred, the area of deformation may be targeted with lidar. Here we present a method whereby it is possible to generate measurements of vertical displacements in the absence of pre-event lidar data. This is achieved by using pre-event optical images and a post-event high-resolution digital elevation model (DEM). The method takes advantage of the fact that there are many archived pre-event satellite images, and that post-event lidar is likely to be flown after an earthquake.

We test this methodology in the case of the M_w 7.2 El Mayor-Cucapah earthquake and compare the results with the results of the differencing technique (Oskin *et al.* 2012). Wei *et al.* (2011), using optical satellite imagery, InSAR and seismology, have calculated a kinematic model of the earthquake. They found that a rupture 120 km long that propagated both to the north-west of the epicentre through the Sierra Cucapah and to the south-east on the newly identified Indiviso fault. Due to data availability (lack of suitable

SPOT scenes in the southern part of that region), we restrict our study to that of the vertical displacements due to rupture on the faults in the Sierra Cucapah region north of the epicentre.

2 VERTICAL DISPLACEMENTS FROM APPARENT HORIZONTAL DISPLACEMENTS

To estimate vertical displacements we make use of two pre-event, stereoscopic satellite images and a high accuracy post-event lidar DEM. The geometrical principle behind the method is illustrated in Fig. 1 for the simple case in which a flat land surface is imaged by two satellites before an earthquake and then undergoes uniform vertical uplift on one side of a fault. Orthorectification, the process by which geometrical distortions caused by terrain relief are removed, projects points from the raw satellite images onto a reference plane. In this process, a DEM is used in order to project the points into the correct location, creating a planimetric image (Kraus 1992; Novak 1992). However, the images were acquired before the vertical uplift had occurred; if they are then orthorectified with a DEM generated after the earthquake, the orthorectified images will contain an error. A given point will not project onto its location before the earthquake (B′ in Fig. 1), but will be displaced (B1 and B2 in Fig. 1). The apparent horizontal displacements between the two images at each point can be estimated using image cross-correlation with sub-pixel resolution (by measuring distance d in Fig. 1), and will reflect the topographic change contained in the post-earthquake DEM (Fig. 1). Making use of the sine rule, the apparent horizontal displacement d is related to the change in height h in this simple example by

$$h = d\frac{\cos i_1 \cos i_2}{\sin(i_1 + i_2)} \tag{1}$$

where i_1 and i_2 are the incidence angles in the two images. SPOT's pushbroom style measurements give rise to a linear central projection (i.e. each scan line has independent central projection), rather than a central projection for the entire image. The parallax due to height changes should be estimated in the scan line direction. Given the near north-south satellite tracks, the stereoscopic effect will produce much larger apparent east-west displacements than those in the north-south direction. This is further discussed in more detail in Section 3.5. In the real case examined in Section 3, one of the two images has a near-nadir incidence angle, that is $i_1 \approx 0$. In this case eq. (1) reduces to $h = d \cot i_2$. This geometry is less favourable due to a smaller base-to-height ratio; however, the estimation of apparent horizontal displacements is still possible with image cross-correlation with sub-pixel resolution (Morgan *et al.* 2008).

In general, heights will vary from point-to-point and we require expressions for vertical displacements when they occur on sloping terrain (Fig. 2); the gradient of heights λ is positive when heights increase from left to right. As before we assume that image 1 is viewed from the left with incidence angle i_1 and image 2 from the right with incidence angle i_2. A step-by-step derivation of the relationship between the actual vertical displacement and apparent horizontal displacements is given in Appendix C.

$$h = \frac{d\cos(\lambda - i_1)\cos(\lambda + i_2)}{\cos^2\lambda \sin(i_1 + i_2)} \tag{2}$$

where $h = \overline{AH}$ and $d = \overline{GF}$ in Fig. 2. The apparent asymmetry between the terms in the numerator of eq. (2) results from measuring the incidence angles in opposite senses in Fig. 2.

In an earthquake, the earth's surface undergoes both horizontal and vertical displacements. In the presence of pre-existing topographic relief, the horizontal displacements will produce changes

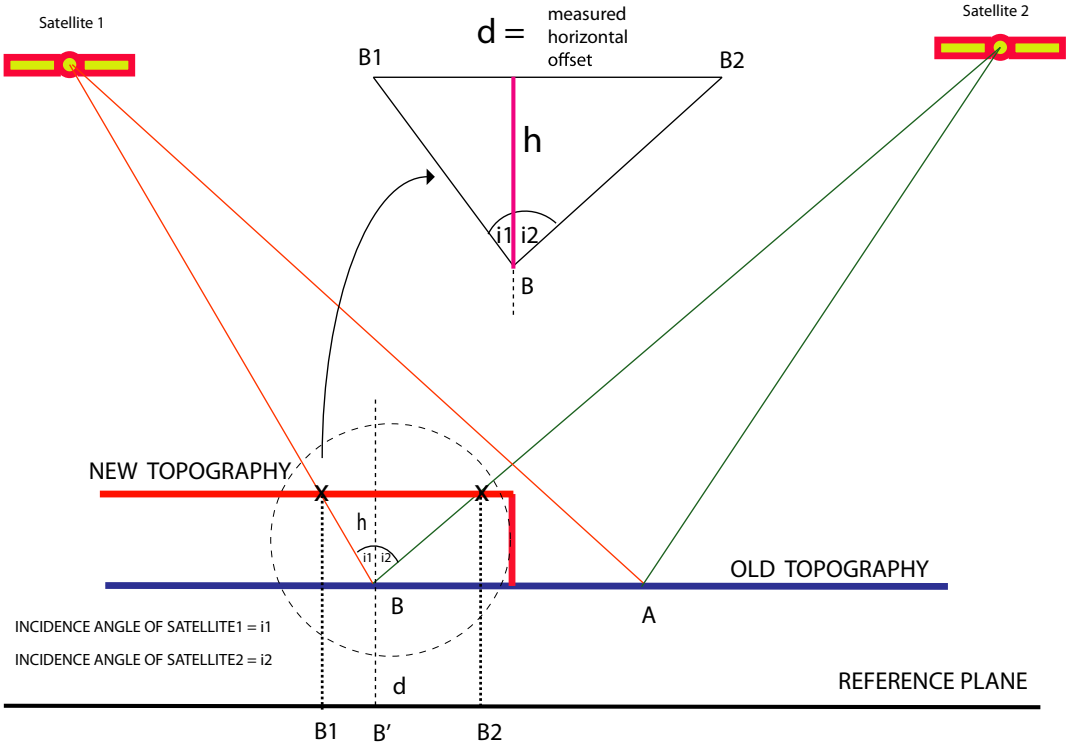

Figure 1. Sketch showing the geometry for orthorectification in a simple example where both images obtained before the event have large incidence angles. The red line represents the new topography in this example, and the blue line represents the original heights when the images were acquired. Point B has undergone a vertical displacement, whereas point A is unchanged.

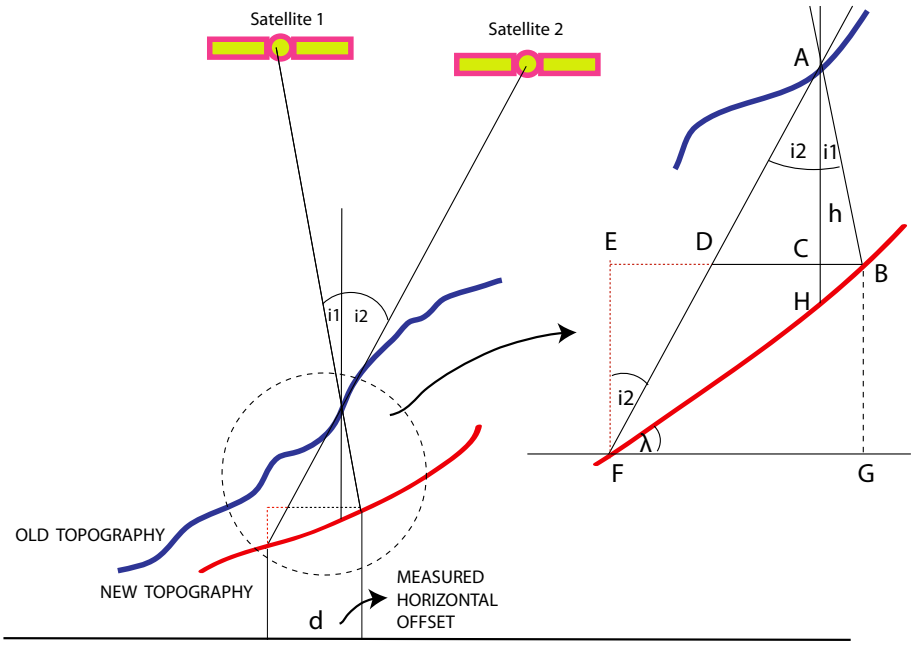

Figure 2. Sketch showing the geometry of orthorectification for the case of vertical displacement on a slope.

in height through the advection of topography. The total change in height Dh at a point is made of two components:

$$Dh = \delta h + \mathbf{u} \cdot \nabla h \tag{3}$$

where $\mathbf{u}$ is the horizontal displacement vector. The first component is the actual vertical displacement at that point and the second component the height change resulting from the advection of topography. Assuming the horizontal displacements have been estimated, the true vertical displacement can be obtained from the total height change by

$$\delta h = Dh - \mathbf{u} \cdot \nabla h. \tag{4}$$

Eq. (4) may be used to correct a post-event lidar DEM to produce a DEM that differs from the pre-event topography only by the vertical displacements. When the images are orthorectified using this corrected DEM, the apparent horizontal displacements will provide estimates of the vertical displacements alone.

2.1 Algorithm overview

Here we outline the steps employed to derive vertical displacements. In order to keep the description of each step concise, we defer more detailed technical explanations to later in the text. A full work flow diagram summarizing the processing required is given in Fig. A1 in Appendix A.

Step 1. The pre-event image is orthorectified with the aid of Ground Control Points (GCPs) located on a reference map (e.g. a shaded DEM) with properly registered horizontal coordinates. The post-event image is orthorectified using tie-points identified on the first (pre-event) orthorectified image. For the near-nadir images used to obtain horizontal displacements, topographic artefacts will be small and non-lidar DEMs with coverage across the whole of the image (e.g. a SPOT DEM) can be used.

Step 2. Horizontal displacements are estimated by applying image cross-correlation with sub-pixel resolution to pre-event and post-event nadir images using the freely available software *Cosi-cor* (www.tectonics.caltech.edu/slip_history/spot_coseis/download_software.html). All displacement maps obtained by *Cori-corr* have a certain degree of long wavelength error present that needs to be removed before proceeding to the next step. The source and nature of the long wavelength error is discussed in Section 3.2.2.

Step 3. The horizontal displacements are used to remove the advective component of height change from the post-event lidar DEM. Instead of implementing eq. (4) we use a Lagrangian approach. For each grid point in the post-event lidar DEM, we calculate the horizontal coordinates it had before the displacement $\mathbf{u}$ and then resample the DEM onto a regular grid.

Step 4. The corrected post-event lidar DEM is used to orthorectify two stereoscopic pre-event images acquired at different times with a large incidence angle difference. In order to obtain a DEM over the whole area of the images, as required by the *Cosi-corr* orthorectification scheme, the post-seismic lidar DEM was mosaicked with a DEM generated using SPOT5 stereo-pairs (see Section 3.4).

Step 5. Apparent horizontal displacements due to the vertical displacements are calculated by image cross-correlation with sub-pixel resolution of the two pre-event images using *Cosi-corr*. The GCPs and tie-points used in orthorectifying these images were placed only within the region of the post-event lidar to keep the registration of the images tied precisely to the post-event lidar. Placing the tie points within the deformation zone results in a long-wavelength error that must be removed.

Step 6. Apparent horizontal displacements are converted to vertical displacements using eq. (2).

3 CASE STUDY OF THE M_w 7.2 2010 EL MAYOR-CUCAPAH EARTHQUAKE

This section describes the processing steps in detail for the case of the M_w 7.2, 2010 El Mayor-Cucapah earthquake.

3.1 Data sets

There are two lidar DEM data sets of this area (Table 1). The pre-earthquake lidar DEM has 5 m spatial resolution and broad coverage

Table 1. Pre-event and post-event lidar DEM for El Mayor-Cucapah region.

DEM	Date	Points/m^2	Spatial resolution	Elev. accuracy [cm]
Pre-earthquake	2006 August	N/A	5 m	N/A
Post-earthquake	2010 August	9	1 m	5–30

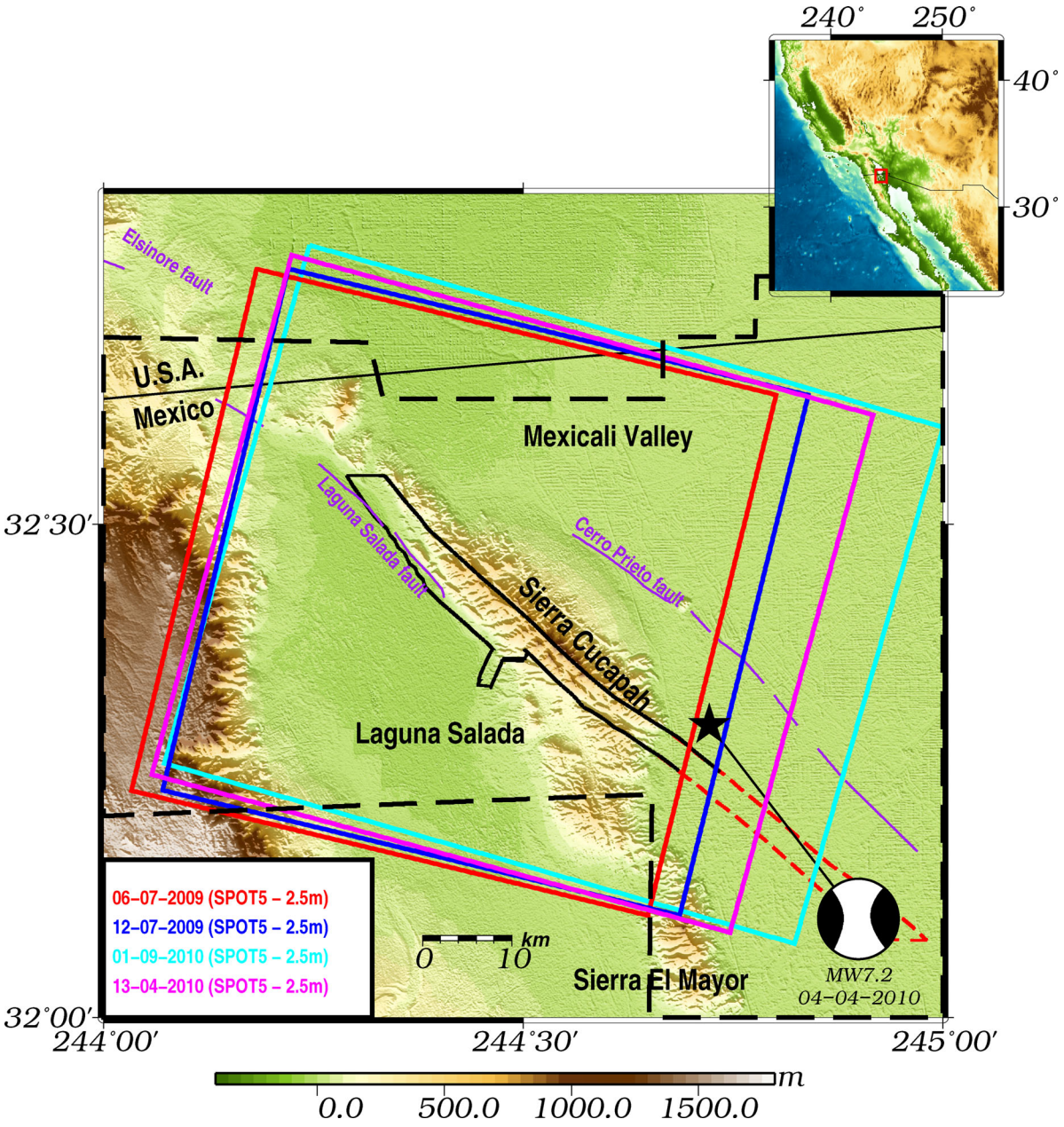

Figure 3. Topographic map of the epicentral area of the 2010 M_w7.2 El Mayor-Cucapah earthquake. The dark blue, light blue, magenta and red rectangular boxes show the areas covered by the SPOT panchromatic images used in this study (Table 2). The narrow black polygon marks the area covered by the post-earthquake lidar 1 m resolution DEM used in this study. The dashed red polygon, which is a continuation of the black one, shows the extent of the post-earthquake lidar data set not used in this study. The black dashed polygon marks the area covered by the pre-earthquake lidar 5 m resolution DEM. The focal mechanism of the earthquake is from the USGS. The inset shows the location of this figure within southwestern North America. The purple lines show the locations of faults in the region.

(Fig. 3). The post-event lidar DEM, with 1 m spatial resolution, was acquired in 2010 August, four months after the earthquake. It covers a narrow strip along the earthquake rupture as outlined in Fig. 3. The post-event lidar DEM is used in the estimation of vertical displacements around the fault as described above. In addition, we use differences between the two lidar DEMs, as described in Oskin *et al.* (2012), to validate the vertical displacements estimated from image matching, except that here we first correct for the effects of the horizontal advection of topography.

We make use of four panchromatic SPOT5 2.5 m images at different steps in the analysis outlined above (Table 2, Fig. 3). From these images, we selected three image pairs with different viewing

Table 2. SPOT scenes used in the study of the $M_w = 7.2$ 2010-04-04 El Mayor-Cucapah earthquake.

Date	SPOT satellite	Spatial res. m	Incidence deg°	Sun Azimuth deg°	Sun elev. deg°
2009-07-06	SPOT5	2.5	24	161	39
2009-07-12	SPOT5	2.5	−0.78	114	69
2010-04-13	SPOT5	2.5	20	146	63
2010-09-01	SPOT5	2.5	−0.77	141	61

Table 3. Stereo-pairs formed from the SPOT scenes and used in the study of the $M_w = 7.2$ 2010 El Mayor-Cucapah earthquake. Date order reflects the pre-event and post-event image used in matching, even though they are not always used in the chronological order as the images with large incidence angles are used as post-event images.

Stereo-pair name	Dates of the two images	Function
Pair A	2009-07-12 and 2010-09-01	Horizontal displacements
Pair B	2009-07-12 and 2009-07-09	Vertical displacements and DEM generation
Pair C	2010-09-01 and 2010-04-13	DEM generation

geometries (Table 3). Pair A is formed from two near-nadir images, one acquired before the earthquake (2009-07-12) and the other after the earthquake (2010-09-01) (Table 2). It is used to determine the horizontal displacements occurring in the earthquake. Pair B consists of two pre-event images (2009-07-09/2009-07-12), one of which is obliquely viewed and other is near-nadir. Image matching of this pair provides apparent horizontal displacements and hence estimates of vertical displacements. The third pair (Pair C) is used to construct a 2.5 m resolution DEM in order to orthorectify the images of pair B over their entire area.

3.2 Horizontal displacements

We first determined the horizontal displacements occurring in the earthquake (Fig. 4) using image pair A. Orthorectification and image cross-correlation with sub-pixel resolution were carried out using the *Cosi-corr* software (Leprince *et al.* 2007). The basic methodology is described below; further details may be found in Leprince *et al.* (2007).

3.2.1 Orthorectification

Before image matching can be done, distortions to the images due to oblique viewing of a surface with varying height must be removed. Direct orthorectification determines where the look direction corresponding to each pixel in the image intersects a DEM of the surface, from which its correct geographic location may be determined. The drawback with this method is that it results in an irregularly spaced grid on the ground, the irregularities arising, for example, from topographic relief or variations in satellite attitude. *Cosi-corr* instead employs an indirect orthorectification scheme, whereby a grid on the ground with regularly spaced horizontal coordinates is established, and the corresponding location on the image determined. The intensities at these locations may then be determined by interpolation from the regularly spaced image values.

Whichever method of orthorectification is employed, knowledge of the look direction corresponding to each pixel in the image is required. Errors in these, arising, for example, from errors in determination of the attitude of the spacecraft, can be corrected with the use of GCPs. A GCP is a point in a reference map, where the ground coordinates are known, that can also be identified in the image to be orthorectified. The difference between the satellite look vector, estimated using information about its attitude and the imaging system, and the true look vector, calculated for the known location of the GCP, is given by

$$\vec{\delta u}(x, y) = \vec{u}_{\text{sat}}(x, y) - \vec{u}_{\text{GCP}}(x_0, y_0), \tag{5}$$

where x and y are the coordinates of the GCP in the raw image. The best-fitting linear relationship to the difference in look directions at the GCPs

$$\delta\vec{u}_{\text{corr}}(x, y) = \begin{bmatrix} a_1 & b_1 & c_1 \\ a_2 & b_2 & c_2 \\ a_3 & b_3 & c_3 \end{bmatrix} \begin{bmatrix} x \\ y \\ 1 \end{bmatrix} \tag{6}$$

may be determined and used to correct the look vectors across the whole image (Leprince *et al.* 2007). Here $\delta\vec{u}_{\text{corr}}$ is the look vector correction, and a_i, b_i and c_i are constants for each coordinate direction, $i = 1$, 2 and 3. In this case, the reference image used was a shaded relief map derived from a 20 m resolution SPOT DEM obtained though the ISIS programme (http://www.isis-cnes.fr/). In order to facilitate the identification of GCPs, the shaded relief map was constructed for sun angles the same as those at the time of the pre-event SPOT image acquisition. We identified a minimum of 15 GCPs uniformly distributed over the area of the pre-event SPOT image and the shaded relief map (Leprince *et al.* 2007).

In ortho-rectifying the post-event image, a correction for the look vectors is carried out in a similar fashion to that above for the pre-event image, but in this case using a set of tie-points. These are identical points in the post-event image and the pre-event image for which the ground coordinates are now known. To minimize the effects of movement of the tie points due to the earthquake, we identified 10 tie-points in the two images distributed uniformly over peripheral areas where the deformation was likely to be smallest. It should be noted that the pre-event and post-event SPOT scenes used here have very small incidence angles (−0.78°, −0.77°), so that any short wavelength artefacts due to high relief should be small. Table 4 lists the smallest topographic error that would result in a positional error of one pixel.

3.2.2 Image matching

The *Cosi-corr* software estimates horizontal displacements between the orthorectified pre-event and post-event images by cross-correlation of small windows of data in the two images. The cross-correlation is carried out in the frequency domain and sub-pixel

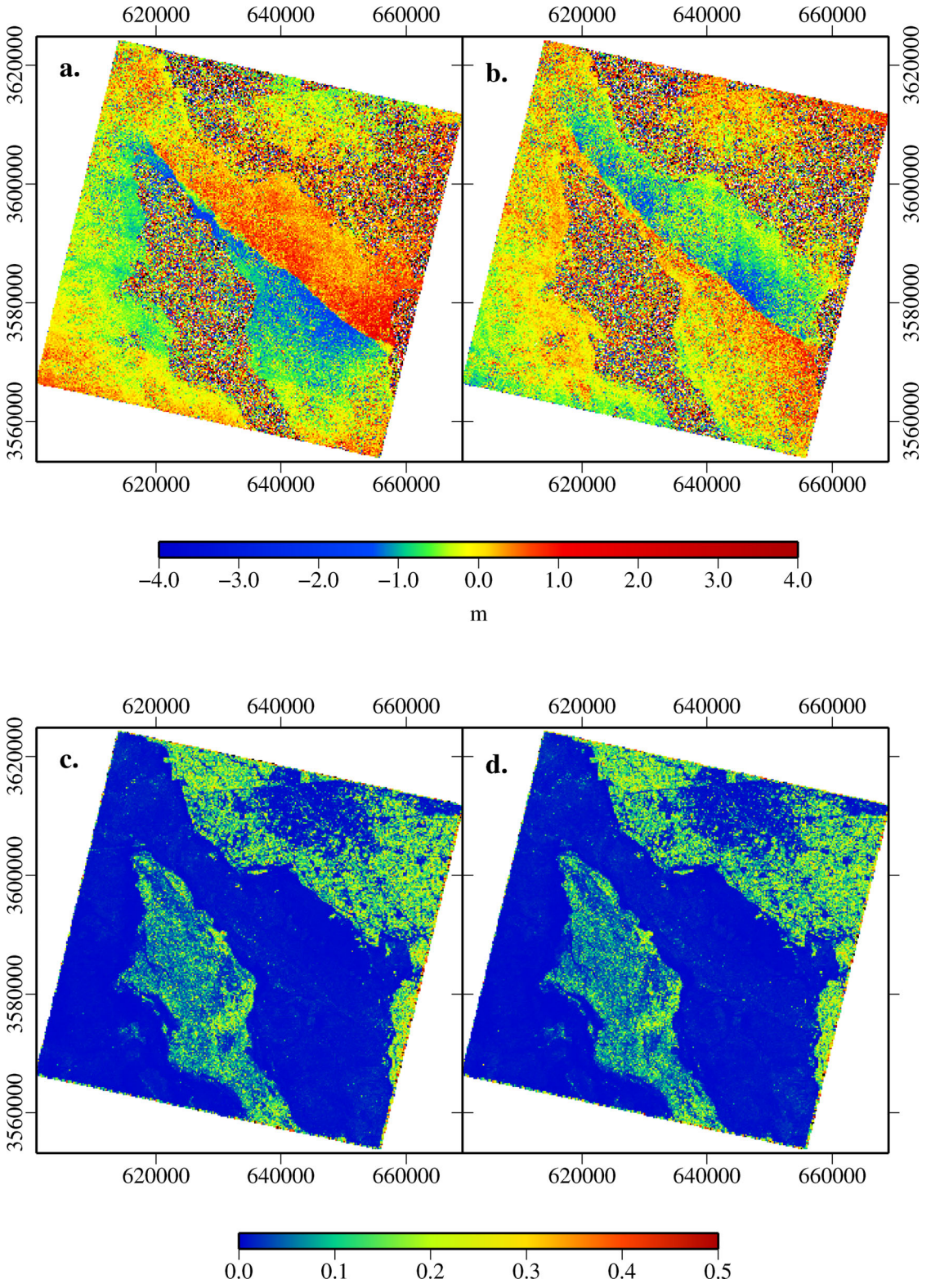

Figure 4. Horizontal displacement maps for the El Mayor-Cucapah earthquake. (a) E–W component and (b) N–S component; (c) and (d) show normalized rms variability for E–W and N–S displacements. The normalized rms values for the displacement maps are obtained by dividing the image into windows of 5 × 5 pixels in size, calculating the rms for each window and then dividing all the values by maximum rms value for that image.

resolution in the displacement estimates obtained by using the variations in phase differences as a function of frequency. Variations of phase in the x direction yields east–west displacements and those in y direction north–south displacements. The size of the window used in the cross-correlation determines the area from which a single measurement of east–west and north–south displacement is derived, and hence the measured displacements represent an average value over the window area. Small windows provide higher resolution, but

Table 4. Vertical DEM errors for SPOT5 before the positional error is bigger than a whole pixel. i is incidence angle and dh is a vertical error.

i°	1	5	10	15	20	25	27
dh (m)	140	28	14	9	7	5.5	5

noisier measurements. Empirically, we find a window size of 32×32 pixels (the pixel size is 2.5 m) provides a reasonable signal-to-noise ratio.

The window is stepped at constant increments over the image to obtain displacement estimates on a regular grid. Commonly, an increment of half the window size is used. However, because we need to compare the vertical displacements derived here with the results of differencing the two lidar data sets, we used a smaller increment of 4 pixels, that is a grid spacing of 10 m, and also resampled the lidar differences to 10 m. The smaller increment size means that errors between neighbouring grid points will be more highly correlated.

The displacement estimates after image matching initially contain a long wavelength error, to a good approximation a bias and tilt. One cause of this long-wavelength error is errors in the correction for the look vectors in orthorectifying the post-event image. Given the small size of the image, it is not possible to completely avoid the effects of displacement on the tie-points, and errors in the tie-point coordinates will result in errors in the linear coefficients in eq. (6). The long-wavelength error is removed by estimating a linear relationship $u = Ax + By + C$, where u is the displacement, x and y are horizontal coordinates, and A, B and C are constants, that best fits each component of displacement in the far field, that is at distances from the fault where displacements due to the earthquake are as small as possible. Displacements from this linear relationship are then subtracted from the initial estimates. We find that the gradient of the linear plane can vary from few centimetres to few metres per hundred kilometres.

The E–W and N–S components of the horizontal displacements are shown in Figs 4(a) and (b). They show a clear discontinuity which represents the rupture of the El Mayor-Cucapah earthquake in its northern segment. The average slip at the surface is 2 m with a maximum slip of 3 m, in agreement with the results of Wei *et al.* (2011). There are large areas of decorrelation in the southwest and northeast parts of the maps (Figs 4c and d). The former are due to modifications of the desert in the Laguna Salada during the 14 months interval between images, and the latter due to agricultural activity in the Mexicali Valley.

3.3 Removal of topographic advection from the post-event lidar DEM

The post-event lidar DEM contains height changes relative to pre-event topography due to the horizontal advection of topographic relief as well as vertical displacement (eq. 3). To remove the advection component from the post-event DEM, we first resample the DEM and E–W/N–S displacement fields on the same uniform 2.5 m grid, then calculate the pre-earthquake horizontal coordinates for each node of the DEM by subtracting corresponding E–W and N–S displacements. This corrected post-event DEM on an irregular grid is then resampled onto a uniform 2.5 m grid.

3.4 A composite DEM

In order to obtain the apparent horizontal displacements for the pre-event image pair B resulting from the vertical displacements we must first orthorectify the images. We are only interested in these displacements for the area of the high-resolution post-earthquake lidar DEM. However, *Cosi-corr* requires full DEM coverage of each image as the orthorectification algorithm initializes the process at the four corners of the image (Leprince *et al.* 2007). For the area outside that of the post-event lidar, we derived DEMs with a 2.5 m posting by applying ENVI's DEM generation module (www.exelisvis.com/envi) to both image pairs B and C (Table 3), then combining them in order to minimize areas of decorrelation, This DEM was supplemented for a small strip in the south with the pre-event lidar DEM to achieve full coverage for both images. We then mosaicked this DEM with the post-earthquake lidar DEM, using the latter for the area around the fault. We note that each constituent DEM in the composite DEM has been geo-registered differently and therefore may not be perfectly aligned.

3.5 Vertical displacements

The apparent horizontal displacements between the two pre-earthquake images in pair B were obtained by using *Cosi-corr* software (Leprince *et al.* 2007) to orthorectify the images and match them to sub-pixel accuracy in the same way described in Section 3.2. In orthorectifying the first SPOT image in this pair, we used GCPs identified in a shaded relief map constructed from the composite DEM for sun angles the same as at the time of the image acquisition. In this case, their locations were restricted to the area of the post-event lidar DEM in order to avoid introducing different geo-registration regimes. A long wavelength error correction was made in the same way as for the true horizontal displacements.

Because of the near-polar SPOT orbit—its orbital plane has an azimuth of 8.8° with respect to north at the equator and 13° inclination at 32°N—the north component of the apparent horizontal displacements is much smaller than the east component. If the magnitude of the apparent horizontal displacement is l and the east and north components are e and n, respectively, the total horizontal displacement is given by $l = \sqrt{(e^2 + n^2)}$. However, because the north component is small and relatively noisy, we estimate the magnitude of the apparent horizontal displacement at latitude of 32° to be $l = e/\cos 13^\circ = 1.026e$. Any effect due to departures of the look direction from perpendicular to the satellite track will be negligible. The east component of the apparent horizontal displacement is shown in Appendix B (Fig. B1). Inside the area of the post-earthquake lidar DEM, the accurate DEM ensures accurate geo-correction and orthorectification, whereas outside it we observe large artefacts caused by the mis-registration between the images and DEM. Fig. 5(a) shows the vertical displacements derived as described above and Fig. 5(b) the apparent horizontal displacements, just for the area of the post-earthquake lidar DEM. These figures look similar, (a) being derived from (b) using eq. (2) in Step 6. The pattern of the vertical displacements in the predominantly flat area to the north-west (see also Fig. 8) appears very similar to the results obtained in the Oskin *et al.* (2012) study (Fig. 6). Further south there is a single line of discontinuity that matches the location of the earthquake rupture derived from the horizontal displacements (Fig. 12a).

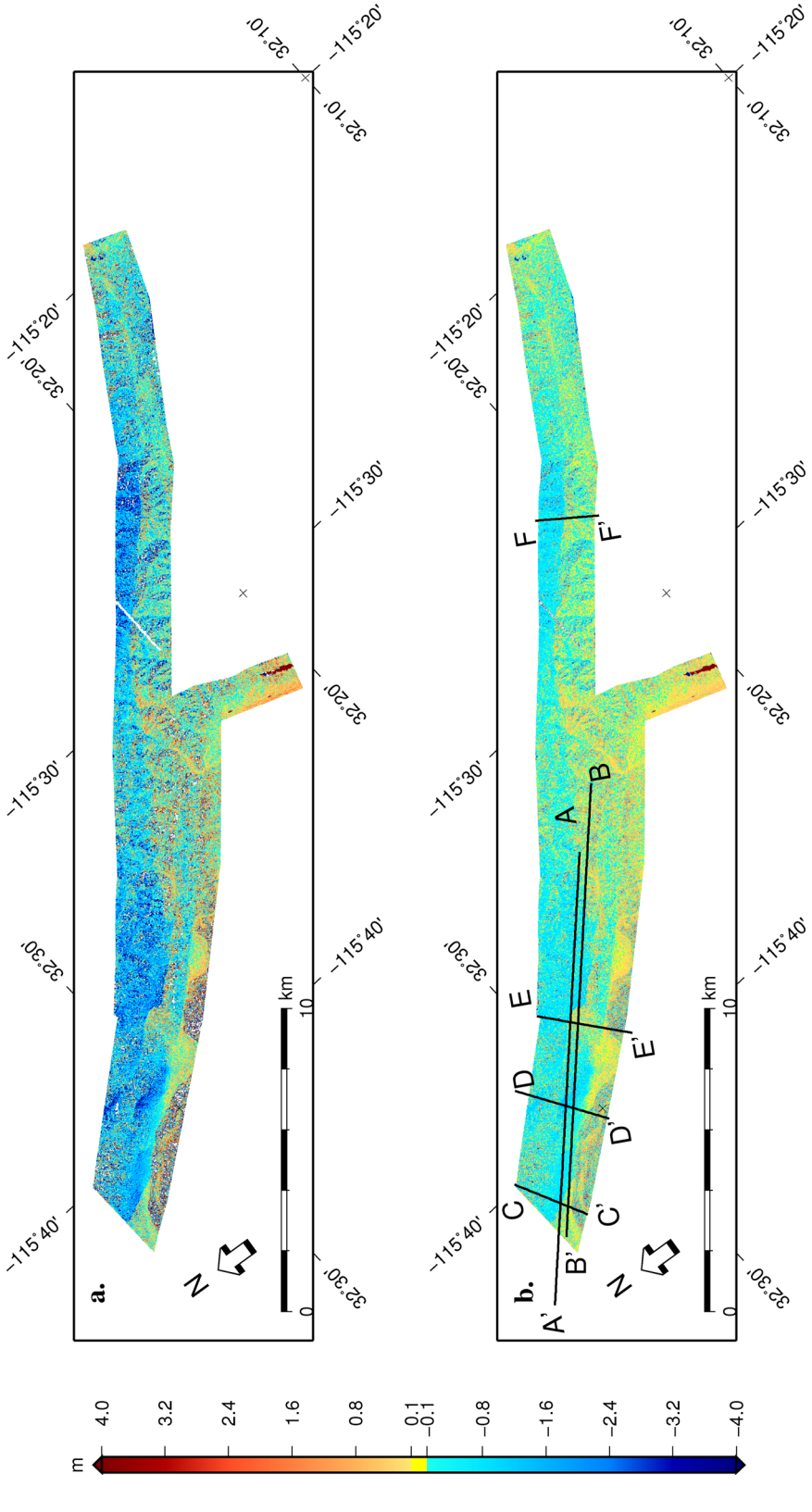

Figure 5. (a) Final calculated vertical displacements. (b) The apparent horizontal displacements for the area of the post-event lidar DEM shown by the black polygon in Fig. B1. Topographic artefacts are small and the main displacement signal is caused by the vertical displacement due to the earthquake. The black lines are locations of the profiles given in Fig. 10.

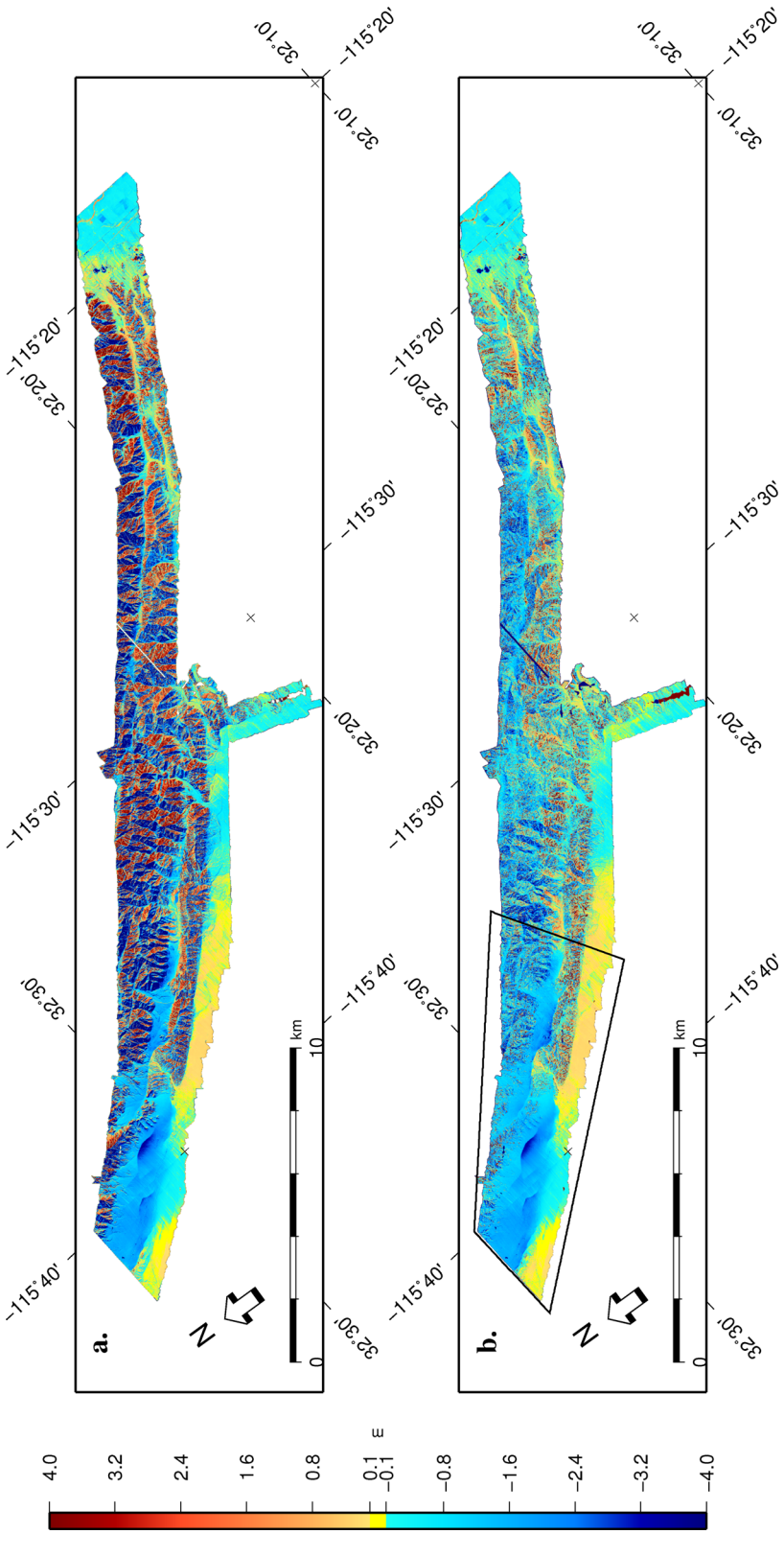

Figure 6. Two difference data sets using the pre-event and post-event lidar DEMs, where the 1 m post-event DEM was resampled to 5 m. (a) Simple difference between the two data sets without allowing for the advection of topography caused by the earthquake (Oskin *et al.* 2012). (b) The same result but the calculated E–W and N–S displacements were used to correct the post-event lidar DEM for advection of topography. The noise is considerably smaller in this case, the topographic artefacts due to the horizontal advection being reduced. The black polygon shows the area covered in Fig. 8.

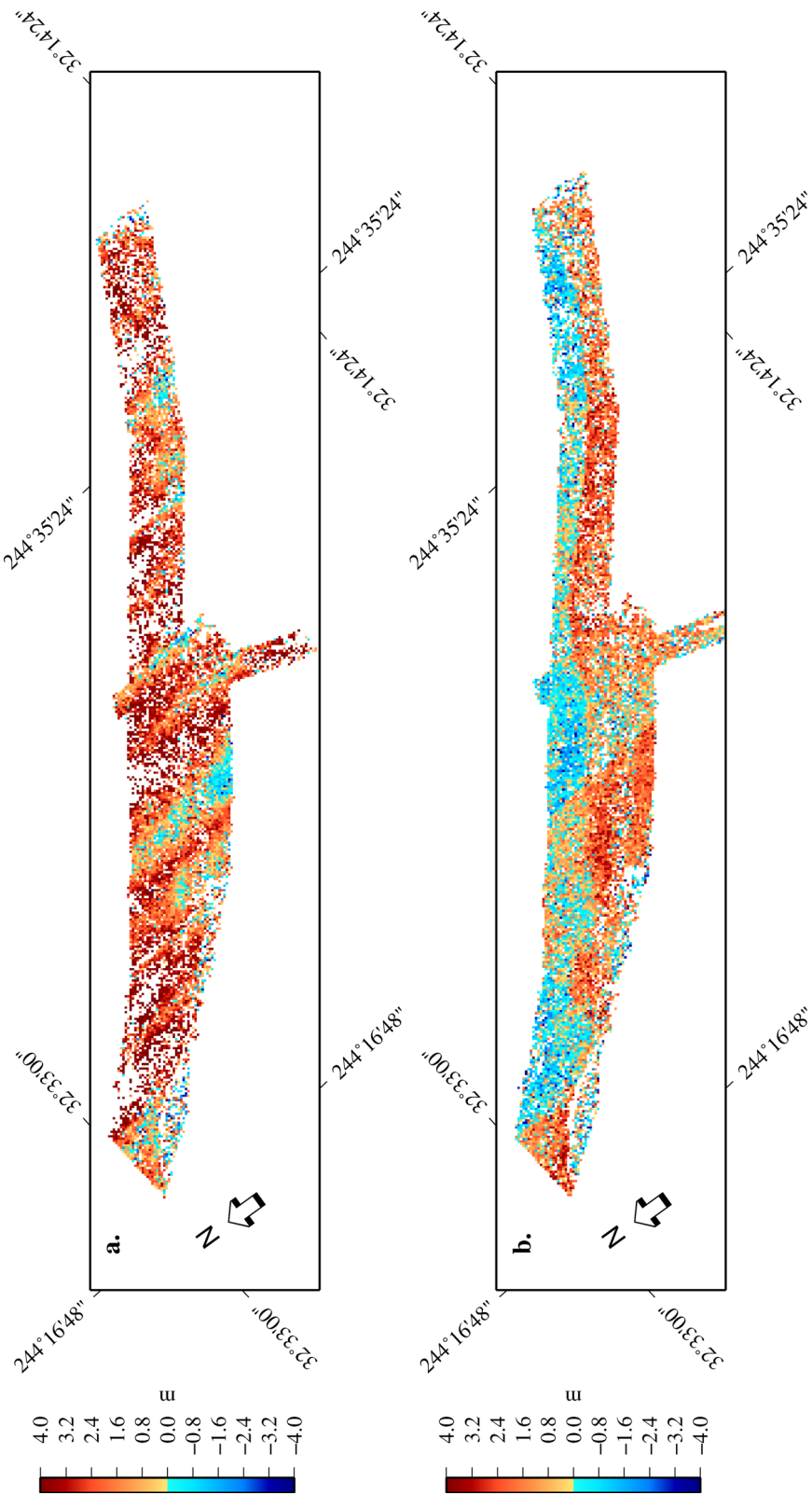

Figure 7. The horizontal displacements as a result of image cross-correlation with sub-pixel resolution of the pre-earthquake and post-earthquake shaded lidar DEM: (a) The N–S component of the horizontal displacement. The striping is caused by the misalignment of the point clouds from the individual flight lines in the pre-event lidar DEM. The N–S displacements alternate between positive and negative displacement reaching a magnitude of 5 m and more in places; (b) The E–W horizontal displacement. The horizontal displacement due to the earthquake is the main signal.

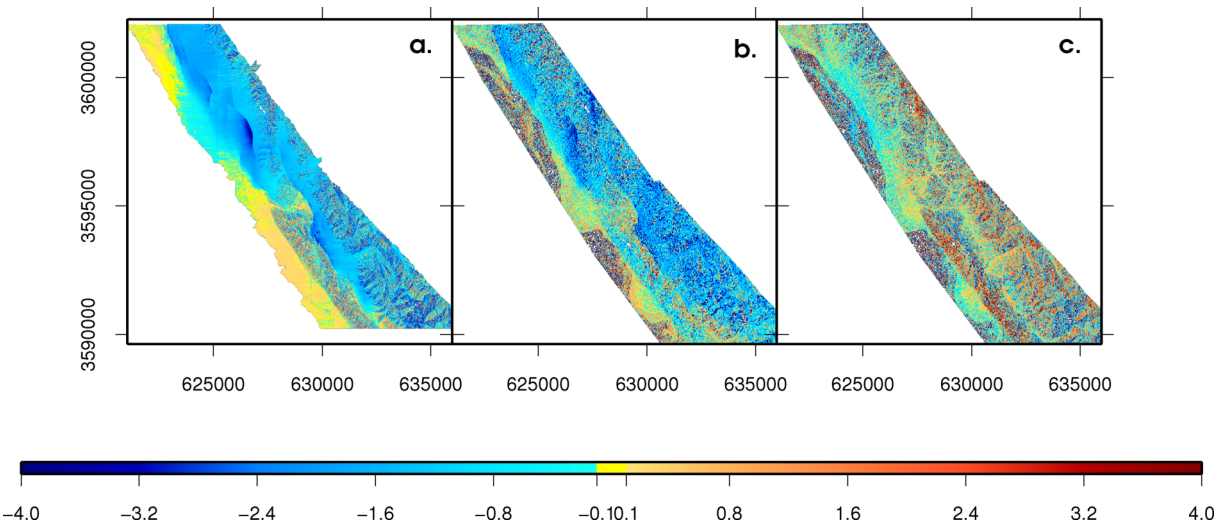

Figure 8. The NW area (black polygon in Fig. 6b) of the post-earthquake lidar used to validate the results of our method versus differencing of the DEMs. (a) Vertical displacements obtained by differencing of pre-earthquake and post-earthquake lidar DEMs, when the post-earthquake lidar DEM was corrected for horizontal advection. (b) Vertical displacements obtained using the method described here. (c) Calculated differences between changes in height from (a) and (b). There is a good agreement between the two estimates of vertical displacement, but both techniques suffer from short wavelength noise although in different locations due to different origins of the short wavelength error.

4 THE VERTICAL DISPLACEMENT FIELD

4.1 Differencing the pre-event and post-event lidar DEMs

We validate the vertical displacements estimated above by comparing our results to the results of differencing the pre-earthquake and post-earthquake lidar data sets. Initially we calculate the difference between these two data sets directly as done in Oskin *et al.* (2012) but, apart from the areas where the slopes are less than 3°, the differences are dominated by effects due to the advection of topography and the vertical displacement signal is obscured (Fig. 6a). We correct the post-event lidar DEM for the horizontal advection of topography as described previously, and then recalculate the difference. The output shows a much clearer signal across the entire field along the fault (Fig. 6b). We observe the distinct signal of a fault that has subsided along its north-east side and uplifted to the south-west, and a branching pattern with many smaller faults in the northeast segment.

Although the recalculated differences are significantly improved, there is still substantial topographic noise. This is partially due to differences in the spatial resolution and mis-registration of the two lidar data sets. The mis-registration can be quantified by directly matching shaded relief derived from the two lidar DEMs. This image cross-correlation with sub-pixel resolution was undertaken using software that we wrote and customized following the methods from Leprince *et al.* (2007); the east and north displacements that result from this matching are shown in Fig. 7. The east–west displacements (Fig. 7b) clearly show the rupture and near field displacement fields, but are also obscured by a few stripes in the N–S direction. However, the north–south component shows a regular striped pattern in the N–S direction (Fig. 7a). This is an artefact resulting from the merging of lidar data on individually flown swaths, the lines directly corresponding to the edges of the flight lines during the point cloud acquisition. Glennie *et al.* (2014) found warping of the scan lines and large systematic errors at the scan-line edges due to the large off-nadir scan angle in the pre-event lidar data set.

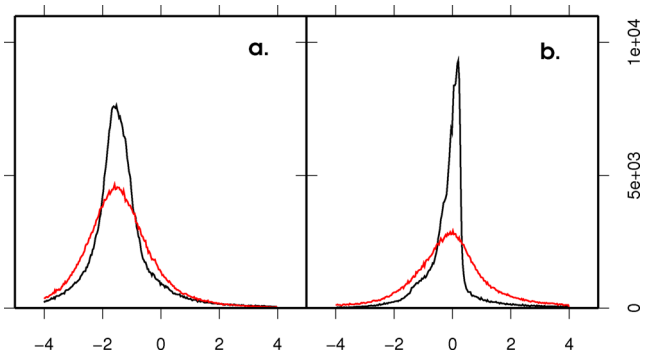

Figure 9. Black lines show histograms for vertical displacements obtained by differencing two DEMs, and red lines show histograms for vertical displacements obtained by our method for the area in Fig. 8. (a) Histograms for hanging-wall area only. Both data sets have the same mean: −1.34 m. The standard deviation for differencing lidar method is 1.05 m and for our method is 1.2 m. (b) Histograms for footwall area. Both histograms have near zero mean. The standard deviation for differencing lidar DEMs is 0.8 m because it is mainly flat relief, and our method is 1.3 m consistent with the hanging-wall area.

4.2 Validation of the vertical displacements

We chose to make a detailed comparison of the differences between the pre- and post-event lidar DEMs and the vertical displacements derived here for the top north-west region of the earthquake rupture. The topography of this area is a mixture of a very flat desert plain and some high relief that is an ideal setting to assess the method. Fig. 8(a) shows a close-up view of the differences between the two DEMs, Fig. 8(b) shows the vertical displacements obtained by the method described in this paper, and Fig. 8(c) is the difference between the two estimates of vertical displacement. They both show the same discontinuities and the same patterns of uplift and subsidence, which agrees with mapped rupture in the field by Fletcher *et al.* (2014) and shown in Fig. 12. Although the differences between these two estimates of vertical displacement are very noisy, there is little remaining signal associated with faulting. Fig. 9(a) compares histograms for the subsidence area north-east from the

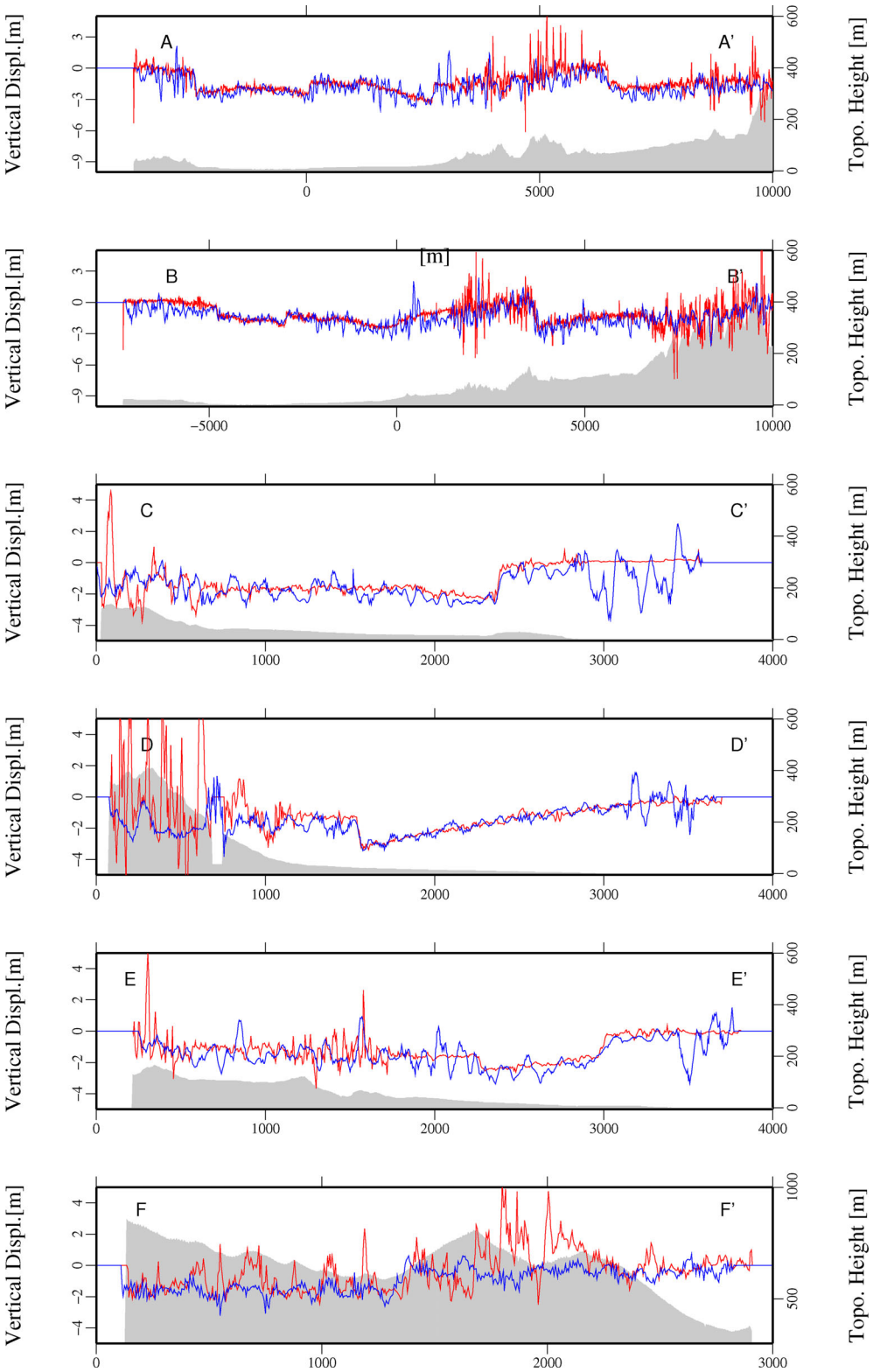

Figure 10. Profiles across the vertical displacement obtained by differencing the two lidar DEMs (red profiles) and the vertical displacements obtained with the method described here (blue profiles). A–A′ and B–B′ profiles are longer profiles running along the long side of the data set, C–C′, D–D′, E–E′, F–F′ profiles are fault-normal (Fig. 5b). The grey areas show the underlying topography.

rupture (hanging-wall area) only. The histogram mean for both data sets is −1.34 m, the standard deviation for the differences between the lidar DEMs is 1.1 m, and the standard deviation for our method is 1.2 m. Fig. 9(b) compares histograms only for the south-west part from the rupture (footwall area). The mean and standard deviation from differencing the lidar DEMs is −11 cm and 0.83 m, respectively, and the mean and standard deviation for our method is −7 cm and 1.31 m, respectively.

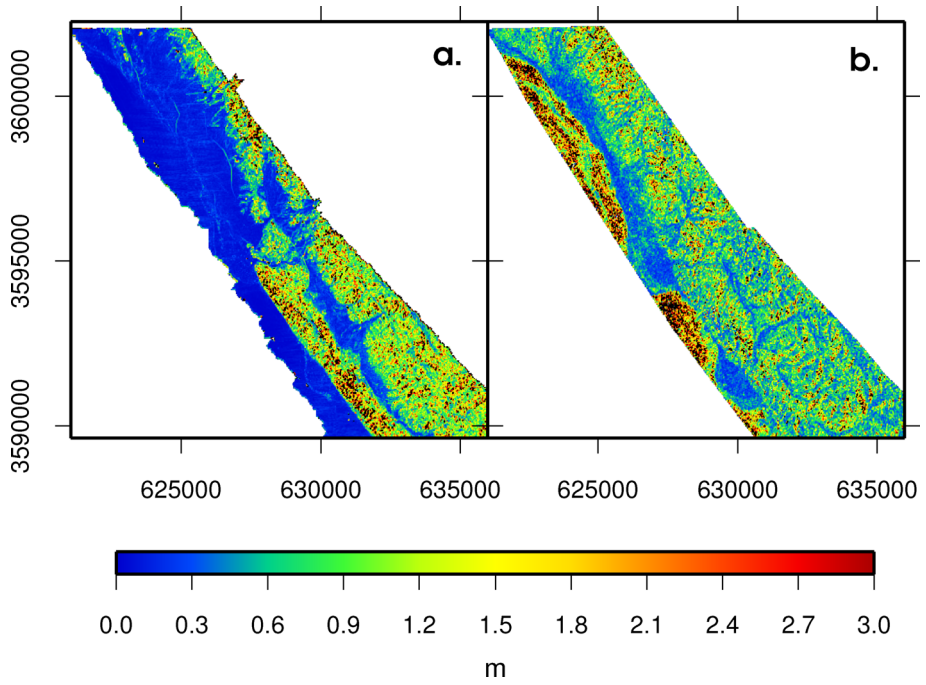

Figure 11. (a) Rms variability for 3 × 3 windows of vertical displacements obtained by differencing lidar DEM for that area of Fig. 8. (b) Rms variability for 3 × 3 windows of vertical displacements obtained by approach introduced in this paper.

A different comparison between the two data sets is made in Fig. 10 along profiles, the locations of which are shown in Fig. 5. Red lines show the differences between the two lidar DEMs including the correction for horizontal advection of topography, and blue lines the vertical displacements obtained by image matching. For the reasons discussed in 4.1 and by Glennie *et al.* (2014), differencing lidar DEMs creates greater short wavelength noise in areas of high topographic relief (Fig. 10), despite the fact that we have removed the height change due to horizontal advection. Also, the study by Nissen *et al.* (2014) shows another example where differencing pre-event and post-event lidars suffer from mis-registration. Our method registers the images used in cross-correlation directly to the lidar DEM which ensures that the topographic artefacts in the vertical displacement field will be minimal. However, the lidar DEM used in our method must not contain systematic errors between scan-lines.

Cross-correlation of images with sub-pixel resolution is very sensitive to changes in image textures, which causes areas of decorrelation. Agricultural, urban and forested land surfaces, or in this case shifting sand, are the major causes of decorrelation which could obscure the signal. The window size, which in our case study is 80 m, is a limiting factor in achieving higher resolution measurements. Fig. 11(a) shows the root mean square error (rms) for 3 × 3 windows for the lidar differences and Fig. 11(b) shows the rms for each 3 × 3 window for our method. The overall rms for our approach is higher than lidar difference for the areas with flat relief, however, more uniform over the whole scene.

5 TECTONICS

The M_w 7.2 Cucapah-El Mayor earthquake occurred on 2010 April 4 in Baja California, Mexico. This tectonically active area links the southern San Andreas Fault zone with spreading of the East Pacific Rise in the Gulf of California (Elders *et al.* 1972). Relative motion between the Pacific and North American plates in the southern San Andreas fault zone is distributed over several major faults (San Jacinto, Elsinore and San Andreas), the motion being dextral strike-slip with a total relative motion of 35–40 mm/year (Johnson *et al.* 1994; Bennett *et al.* 2004). The epicentral area is also characterized by distributed faulting, containing several parallel northeast–southwest dextral strike slip faults with a normal component accommodating extension (Savage *et al.* 1994). It is covered by thick sediments obscuring many of the faults (Pacheco *et al.* 2006). The Cucapah-El Mayor earthquake did not rupture the main plate boundary fault in the area, the Cerro Prieto fault (Fig. 3), but a number of faults to the west of it. The motion on the faults was oblique right lateral (Fielding *et al.* 2010; Fletcher *et al.* 2010; Sandwell *et al.* 2010).

The Sierra Cucapah is bounded to the southwest by the Laguna Salada fault (Fig. 12), the southern extension of the Elsinore fault (Fig. 3; Müeller & Rockwell 1995). It last ruptured in 1892 with an earthquake estimated to have a moment magnitude of M_w 7.2, one of the largest in recorded history in southern California (Hough & Elliot 2004). Although the Laguna Salada fault is located in close proximity to the faults that ruptured, only minor slip, near the USA-Mexico border, was observed. Instead, in the area where we have mapped the vertical displacements, the main rupture seems to have been taken up on the Borrego and Pescadores faults (Axen *et al.* 1999; Fletcher & Spelz 2009). These faults have been mapped as active by Jennings & Saucedo (1994). Wei *et al.* (2011) found that the faults involved in the northwest of the earthquake sequence dipped towards the northeast.

We have overlaid the traces of the active faults mapped by Fletcher & Spelz (2009) in the Sierra Cucapah range over the horizontal displacement map (Fig. 12a) and new traces mapped by Fletcher *et al.* (2014) over the vertical displacement maps for the area of the post-seismic lidar DEM (Fig. 12b). The horizontal displacements show clearly that, as the rupture propagated to the northwest from the epicentre (Wei *et al.* 2011; Uchide *et al.* 2013), it jumped from the Pescadores fault to the Borrego fault through the Puerta Accommodation Zone (Figs 12a and b). Likewise, the discontinuity

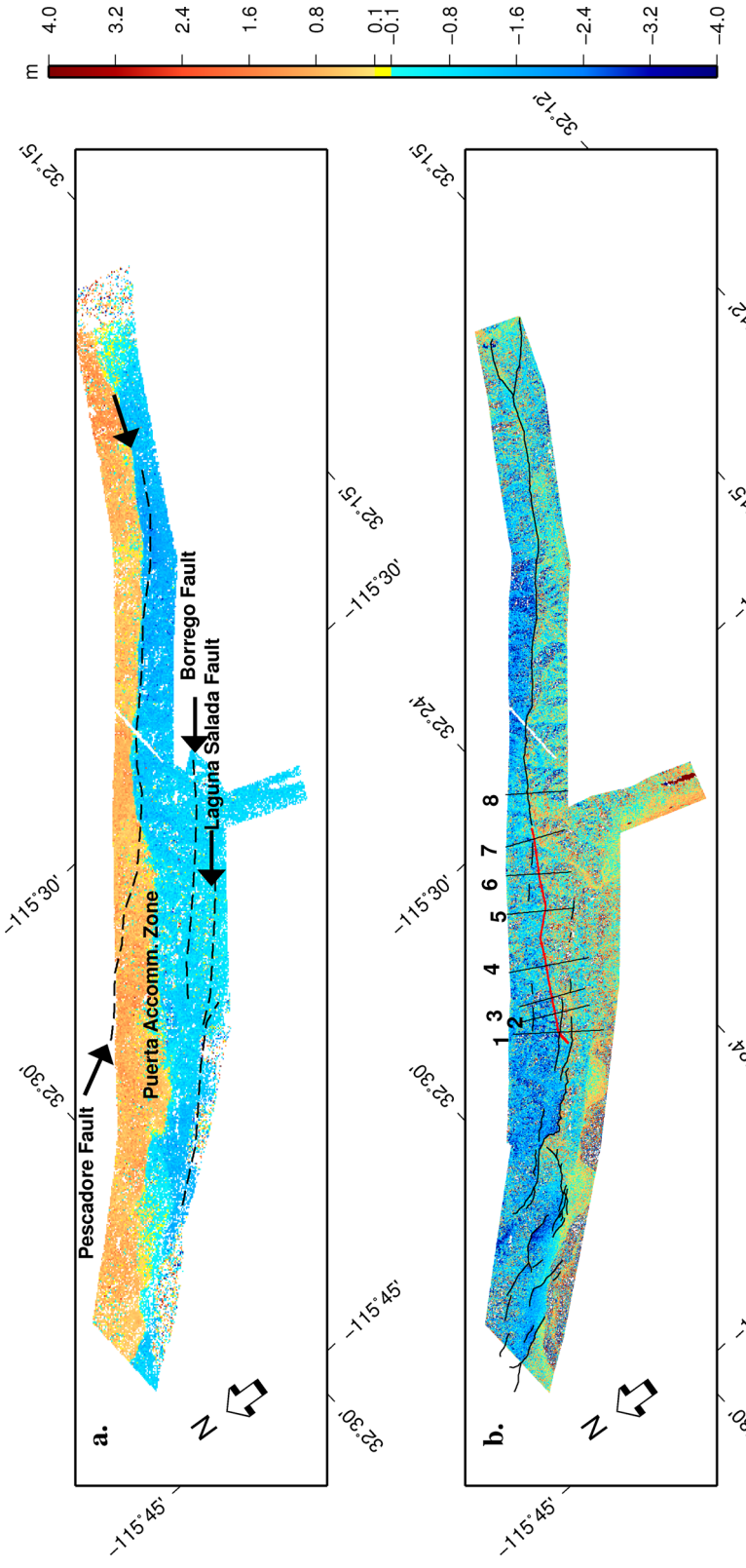

Figure 12. (a) E–W horizontal displacements. Black dashed lines show the faults mapped before the El Mayor-Cucapah earthquake by Fletcher & Spelz (2009) (downloaded from http://response.scec.org/node/273 site in 2010). (b) Vertical displacements for the area of the post-seismic lidar DEM. Black thin solid lines show new fault traces mapped by Fletcher *et al.* (2014) after the earthquake. Red line shows fault trace obtained from the horizontal displacement map that crosses the Puerto Accommodation Zone. Numbered lines denote the location of the topographic profiles shown in Fig. 13.

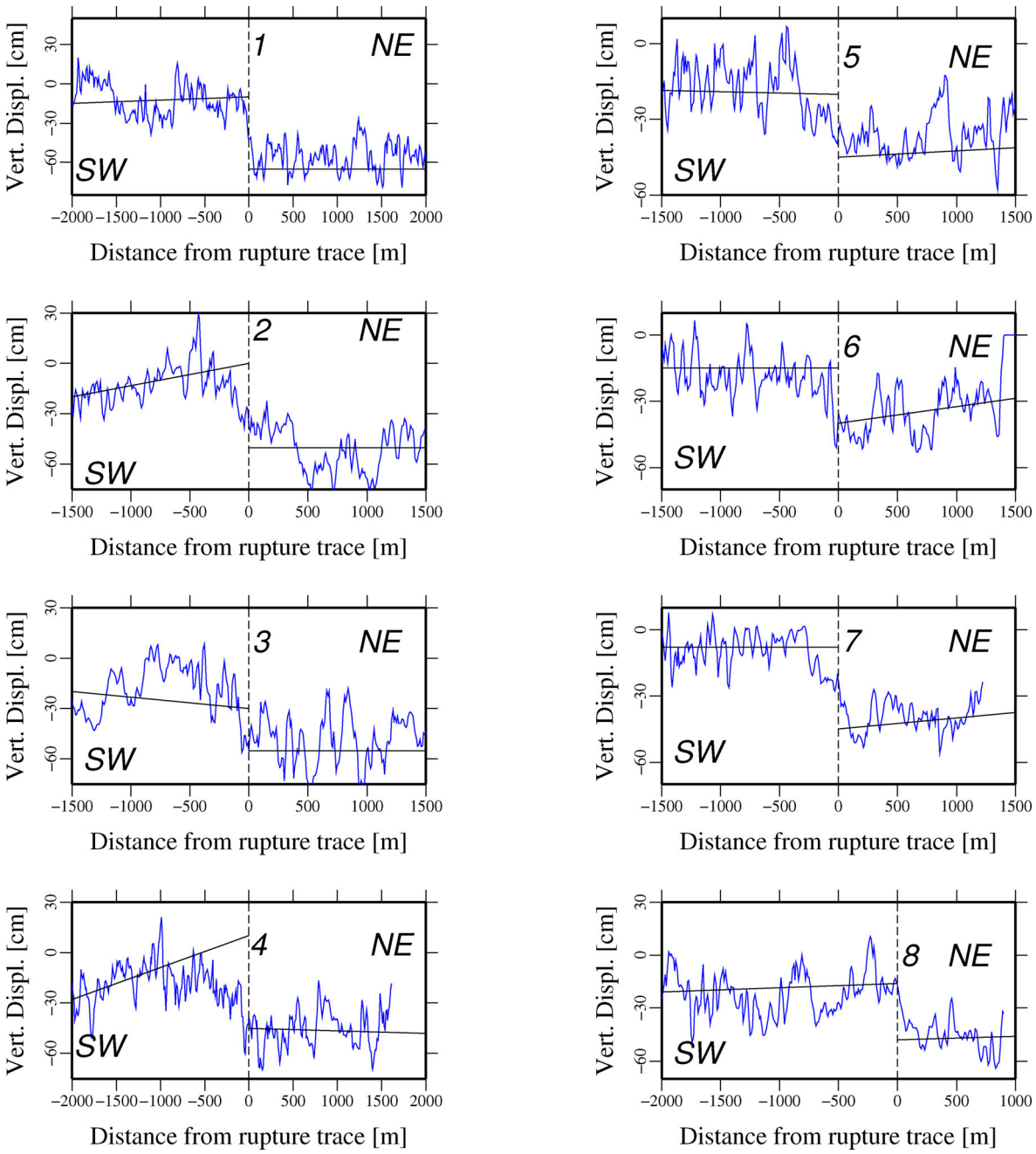

Figure 13. Topography along the profiles indicated in Fig. 12. They have been aligned along the trace of rupture determined from the horizontal displacement map showing the location of the rupture as it goes through the mountains. The straight lines are the best-fitting lines of the topographic profiles on each side of the rupture trace. We used *Cosi-corr*'s Stacking Profile tool.

in the vertical displacement follows the Pescadores fault closely in the southeast (Fig. 12), with a throw down to the northeast, and it can be followed as it crosses the Sierra Cucapah to join the Borrego fault around 32°27′N and 115°36′W.

Although the signal is noisy, topographic profiles (Fig. 13) show a small vertical offset of the order of 20–30 cm in many places at, or close to, the location of the rupture determined from the horizontal displacements as it crosses between the mapped faults. Thus we are able to detect relatively small vertical displacements in an area of rough topography, enabling the rupture to be characterized fully as it crosses the mountains. The sense of motion in the southeast of this area is down to the northeast. In the northwest of the area, where the topographic relief is low, the faulting is distributed across several branches and the vertical displacements on some of these branches switches to down to the southwest. However, the overall subsidence across the area is down to the northeast, in the agreement with the sense of throw on the mapped faults across the Sierra Cucapah (Fletcher & Spelz 2009).

6 CONCLUSION

We have presented a geometrical principle showing how it is possible to determine post-event vertical displacements from one stereo-pair of images acquired before an earthquake and a precise DEM generated after the event. We have then demonstrated this principle in the case of the 2010, M_w 7.2 El Mayor-Cucapah earthquake. The

vertical displacements derived are in agreement with the vertical displacements obtained by differencing the pre-event and the post-event DEMs. The same principle could be applied in the reverse order, for example if a very accurate and precise pre-event DEM exists it can be coupled with a post-event stereo-pair in order to obtain the vertical displacements. We have also demonstrated that with only four satellite archived images we were able to estimate both horizontal and vertical displacements, and derive a DEM of the area. This technique provides aims of directly studying a vertical displacements, using satellite technology, caused by an earthquake or any other tectonic event in regions where a precise and accurate DEM may be available only post-event. Although we have used SPOT5 stereo imagery in this study, other higher-resolution images could equally well be used, for example Worldview or Pleiades.

ACKNOWLEDGEMENTS

Support for this research has been provided by the Natural Environment Research Council through the Centre for the Observation and Modelling of Earthquakes, Volcanos and Tectonics (COMET). The authors would like to thank INEGI (Instituto Nacional de Geografia y Estadistica) for granting access to the pre-event lidar DEM and to OpenTopography.org for expediting access to the post-event lidar data. SPOT images were obtained through ISIS (Incentive for the Scientific use of Images from the Spot system) program, Copyright CNES (2010), Distribution Spot Image S.A. France, all rights reserved. We thank John Elliott, Michael Oskin and an anonymous reviewer for helpful reviews of the manuscript.

REFERENCES

Axen, G.J., Fletcher, J.M., Cowgill, E., Murphy, M., Kapp, P., MacMillan, I., Ramos-Velázquez, E. & Aranda-Gómez, J., 1999. Range-front fault scarps of the Sierra El Mayor, Baja California: formed above an active low-angle normal fault?, *Geology,* **27,** 247–250.

Bennett, R.A., Friedrich, A.M. & Furlong, K.P., 2004. Codependent histories of the San Andreas and San Jacinto fault zones from inversion of fault displacement rates, *Geology,* **32,** 961–964.

Cunningham, D., Grebby, S., Tansey, K., Gosar, A. & Kastelic, V., 2006. Application of airborne LiDAR to mapping seismogenic faults in forested mountainous terrain, southeastern Alps, Slovenia, *Geophys. Res. Lett.,* **33,** L20308, doi:10.1029/2006GL027014.

Duffy, B., Quigley, M., Barrell, D.J., Van Dissen, R., Stahl, T., Leprince, S., McInnes, C. & Bilderback, E., 2013. Fault kinematics and surface deformation across a releasing bend during the 2010 M_w 7.1 Darfield, New Zealand, earthquake revealed by differential lidar and cadastral surveying, *Geol. soc. Am. Bull.,* **125,** 420–431.

Elders, W.A., Rex, R.W., Robinson, P.T., Biehler, S. & Meidav, T., 1972. Crustal spreading in Southern California: the Imperial Valley and the Gulf of California formed by the rifting apart of a continental plate, *Science,* **178,** 15–24.

Fielding, E. *et al.*, 2010. Kinematic fault slip model from joint inversion of teleseismic, GPS, InSAR and subpixel-correlation measurements of the 2010 El Mayor-Cucapah earthquake and postseismic deformation, in *AGU Fall Meeting Abstracts,* Vol. 1, p. 08.

Fletcher, J. *et al.*, 2010. The surface ruptures associated with the El Mayor-Borrego earthquake sequence, *Geological Society of America, Cordilleran section, Abstract LB1-5, Anaheim, California*.

Fletcher, J.M. & Spelz, R.M., 2009. Patterns of Quaternary deformation and rupture propagation associated with an active low-angle normal fault, Laguna Salada, Mexico: evidence of a rolling hinge?, *Geosphere,* **5,** 385–407.

Fletcher, J.M. *et al.*, 2014. Assembly of a large earthquake from a complex fault system: surface rupture kinematics of the 4 April 2010 El Mayor–Cucapah (Mexico) Mw 7.2 earthquake, *Geosphere,* **10,** 797–827.

Glennie, C.L., Hinojosa-Corona, A., Nissen, E., Kusari, A., Oskin, M.E., Arrowsmith, J.R. & Borsa, A., 2014. Optimization of legacy lidar data sets for measuring near-field earthquake displacements, *Geophys. Res. Lett.,* **41,** 3494–3501.

Hough, S.E. & Elliot, A., 2004. Revisiting the 23 February 1892 Laguna Salada earthquake, *Bull. seism. Soc. Am.,* **94,** 1571–1578.

Jennings, C.W. & Saucedo, G.J., 1994. *Fault Activity Map of California and Adjacent Areas, with Locations and Ages of Recent Volcanic Eruptions,* California Department of Conservation, Division of Mines and Geology.

Johnson, H.O., Agnew, D.C. & Wyatt, F.K., 1994. Present-day crustal deformation in southern California, *J. geophys. Res.,* **99,** 23 951–23 974.

Kraus, K., 1992. *Photogrammetry Fundamentals and Processes,* 1st edn, Dummler Verlag.

Leprince, S., Barbot, S., Ayoub, F. & Avouac, J.-P., 2007. Automatic and precise ortho-rectification, co-registration and sub-pixel correlation of satellite images, application to ground deformation measurements, *IEEE Trans. Geosci. Remote Sensing,* **45,** 1529–1557.

Massonnet, D., Rossi, M., Carmona, C., Ardagna, F., Peltzer, G., Feigl, K. & Rabaute, T., 1993. The displacement field of the Landers earthquake mapped by the radar interferometry, *Nature,* **364,** 138–142.

Morgan, G., Liu, J. & Yan, H., 2008. Sub-pixel stereo-matching for DEM generation from narrow baseline stereo imagery, in *Proceedings of the Geoscience Remote Sensing Symposium, Boston, 2008,* Vol. 3, pp. 1284–1287.

Müeller, K.J. & Rockwell, T.K., 1995. Late quaternary activity of the Laguna Salada fault in northern Baja California, Mexico, *Geol. soc. Am. Bull.,* **107,** 8–18.

Nissen, E., Krishnan, A.K., Arrowsmith, J.R. & Saripalli, S., 2012. Three-dimensional surface displacements and rotations from differencing pre- and post-earthquake LiDAR point clouds, *Geophys. Res. Lett.,* **39,** L16301, doi:10.1029/2012GL052460.

Nissen, E., Maruyama, T., Arrowsmith, J.R., Elliott, J.R., Krishnan, A.K., Oskin, M.E. & Saripalli, S., 2014. Coseismic fault zone deformation revealed with differential lidar: examples from japanese M_w 7 intraplate earthquakes, *Earth planet. Sci. Lett.,* **405,** 244–256.

Novak, K., 1992. Rectification of digital imagery, *Photogrammetric Engng. Remote Sensing,* **58,** 339–344.

Oskin, M.E. *et al.*, 2012. Near-field deformation from the El Mayor-Cucapah earthquake revealed by differential lidar, *Science,* **335,** 702–705.

Pacheco, M., Martín-Barajas, A., Elders, W., Espinosa-Cardeña, J.M., Helenes, J. & Segura, A., 2006. Stratigraphy and structure of the Altar basin of NW Sonora: implications for the history of the Colorado river delta and the Salton trough, *Revista Mexicana de Ciencias, Geológicas,* **23,** 1–22.

Sandwell, D.T. *et al.*, 2010. InSAR and GPS measurements of crustal deformation from the El Mayor earthquake: liquefaction and triggered slip, *Cordilleran section, Abstract LB1-8, Anaheim, California*.

Savage, J., Lisowski, M., King, N. & Gross, W., 1994. Strain accumulation along the Laguna Salada fault, Baja California, Mexico, *J. geophys. Res.,* **99,** 18 109–18 116.

Uchide, T., Yao, H. & Shearer, P.M., 2013. Spatio-temporal distribution of fault slip and high-frequency radiation of the 2010 El Mayor-Cucapah, Mexico earthquake, *J. geophys. Res.,* **118,** 1546–1555.

Wei, S. *et al.*, 2011. Superficial simplicity of the 2010 El Mayor-Cucapah earthquake of Baja California in Mexico, *Nature Geosci.,* **4,** 615–618.

Wright, T., Parsons, B. & Lu, Z., 2004. Toward mapping surface deformation in three dimensions using InSAR, *Geophys. Res. Lett.,* **31,** L01607, doi:10.1029/2003GL018827.

Zielke, O., Arrowsmith, J.R., Ludwig, L.G. & Akçiz, S.O., 2010. Slip in the 1857 and earlier large earthquakes along the Carrizo plain, San Andreas fault, *Science,* **327,** 1119–1122.

APPENDIX A

Fig. A1 shows processing steps of the method that we discussed in the text.

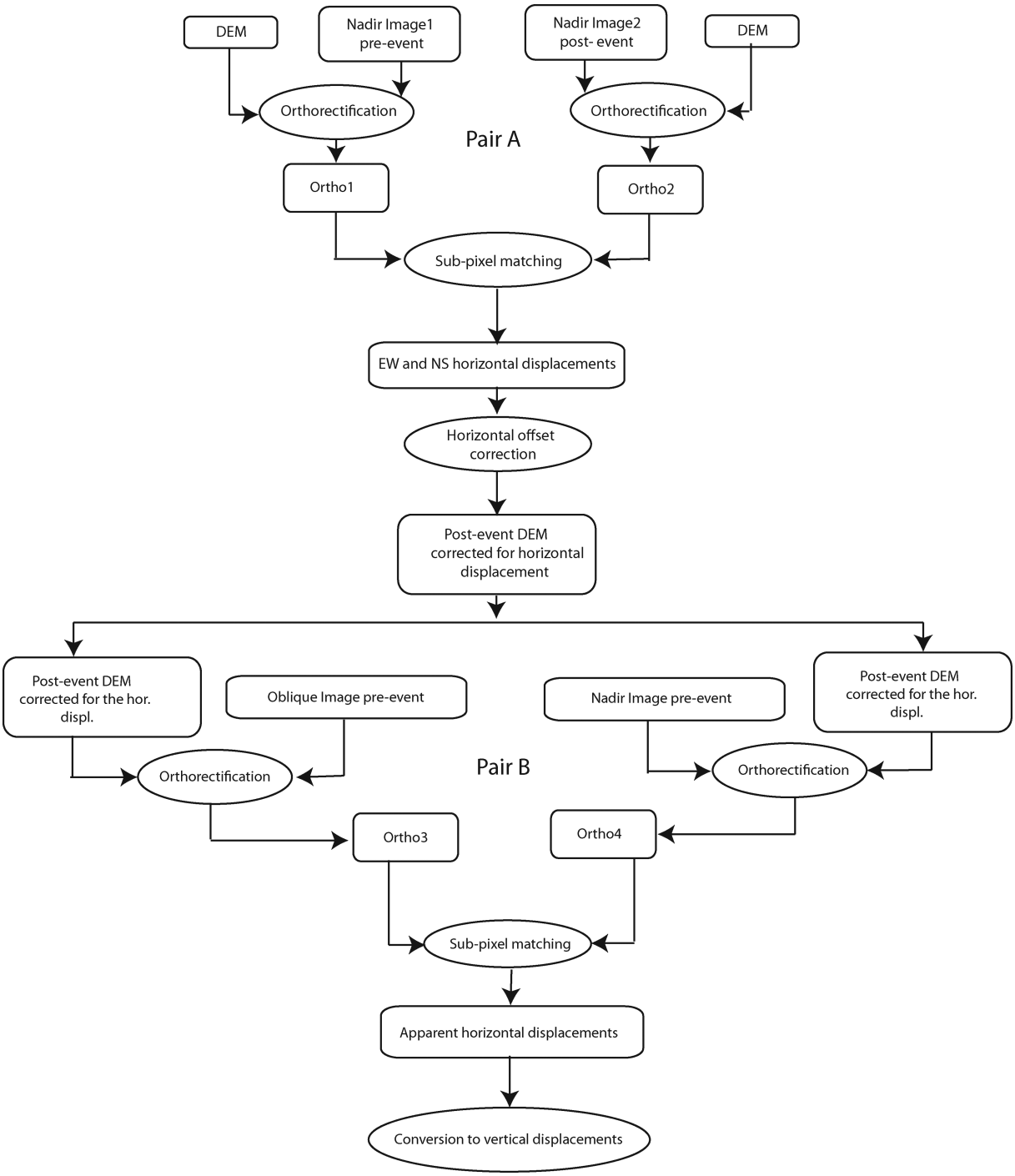

Figure A1. Processing steps and work flow of the method discussed in the text.

APPENDIX B

The EW component of the apparent horizontal displacements obtained by image cross-correlation with sub-pixel resolution of pair B is shown in Fig. B1. Above the top line of the black polygon there is a large area of decorrelation due to the mis-registration of the images outside the post-event lidar coverage. This is apparent in other high relief areas such as areas in the South-West corner and South-East corners of the image. The areas of decorrelation due to the vegetation change cover similar areas to those seen in the matching of pair A (Fig. 4), even though there is only three days between the images in pair B. We used a very small window step during (4 pixels $\times$ 2.5 m) the results of correlation for the regions of high decorrelation resulted in erroneous signal.

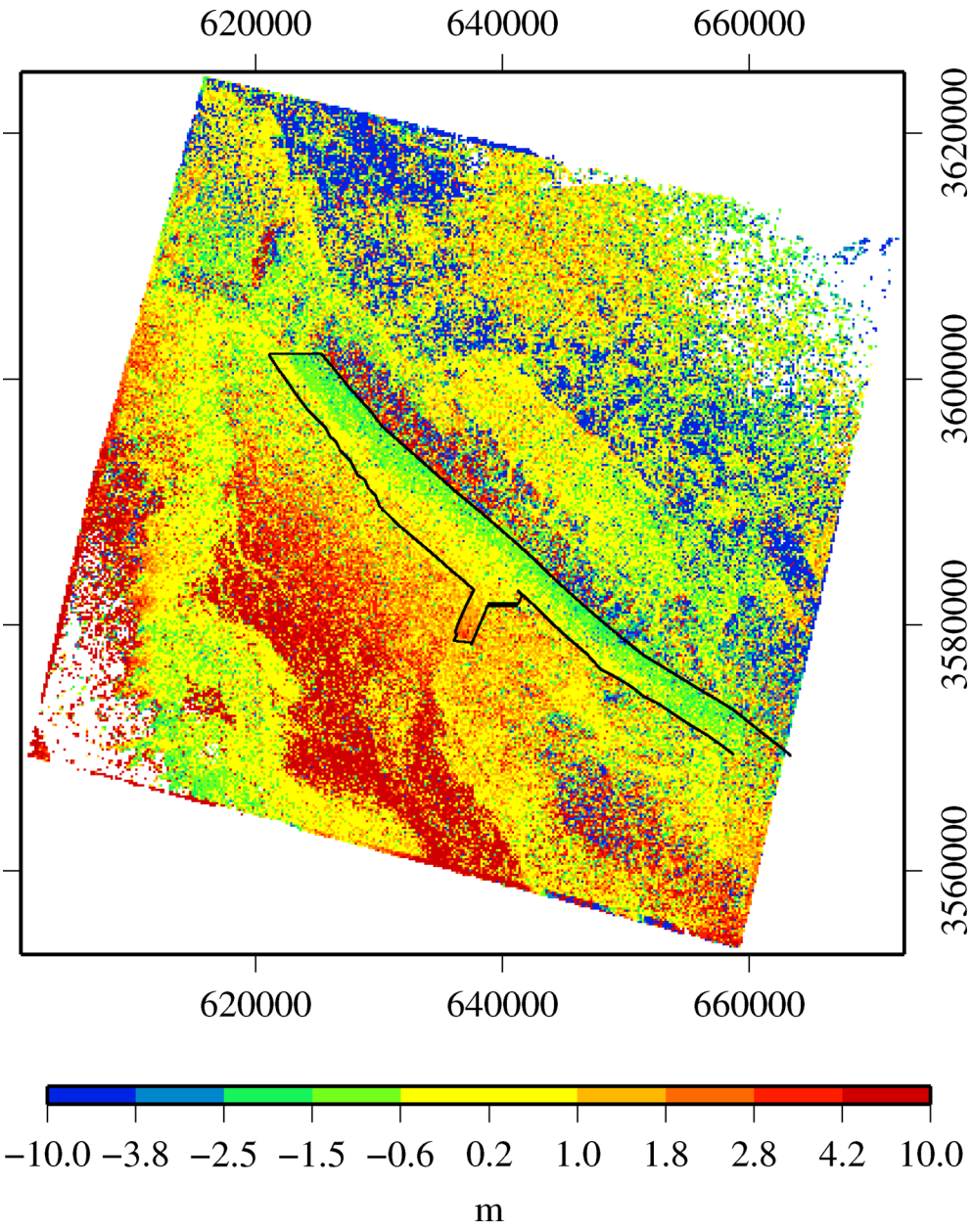

Figure B1. East component of apparent horizontal displacements obtained by image cross-correlation with sub-pixel resolution of the 'B' stereopair. The black polygon delineates the coverage of the post-earthquake lidar.

APPENDIX C

We derive here the expression relating the change in height h to the apparent horizontal displacement d in the presence of a topographic slope λ. The notation follows that given in Fig. 2.

We note that $h = \overline{AH}$ and $d = \overline{FG}$. Applying the sine rule to triangle $\overline{ABH}$

$$\frac{\overline{AH}}{\sin(\lambda + (90 - i_1))} = \frac{\overline{AB}}{\sin(90 - \lambda)} \tag{C1}$$

and hence

$$\overline{AH} = \frac{\overline{AB}\cos(\lambda - i_1)}{\cos\lambda}. \tag{C2}$$

We also have the following expression for $\overline{FG}$:

$$\begin{aligned}\overline{FG} &= \overline{EB} = \overline{ED} + \overline{DB} \\ &= \overline{EF}\tan i_2 + \overline{DB} \\ &= \overline{FG}\tan\lambda\tan i_2 + \overline{DB} \\ &= \frac{\overline{DB}}{(1 - \tan\lambda\tan i_2)}.\end{aligned} \tag{C3}$$

To connect eqs (C2) and (C3) we apply the sine rule to triangle $\overline{ABD}$:

$$\begin{aligned}\frac{\overline{DB}}{\sin(i_1 + i_2)} &= \frac{\overline{AB}}{\sin(90 - i_2)} \\ \overline{AB} &= \frac{\overline{DB}\cos i_2}{\sin(i_1 + i_2)}\end{aligned} \tag{C4}$$

and hence combining eqs (C2), (C3) and (C4), we find that

$$\overline{AH} = \frac{\overline{DB}\cos i_2 \cos(\lambda - i_1)}{\cos\lambda \sin(i_1 + i_2)}$$

$$= \frac{\overline{FG}(1 - \tan\lambda \tan i_2)\cos i_2 \cos(\lambda - i_1)}{\cos\lambda \sin(i_1 + i_2)}$$

$$= \frac{\overline{FG}\cos(\lambda - i_1)\cos(\lambda + i_2)}{\cos^2\lambda \sin(i_1 + i_2)} \tag{C5}$$

The lack of perfect symmetry with respect to an exchange of i_1 and i_2 results from the fact that, as defined in Fig. 2, angle i_2 is measured clockwise from the vertical whereas angles i_1 and λ are measured anticlockwise. When $\lambda = 0$, the expression in eq. (C5) reduces to that in eq. (1) as expected.